

Revisiting CMSSM with Non-Universal Gaugino Masses under Current Constraints

Yabo Dong,^{1,*} Kun Wang,^{2,†} Hailong Yuan,¹ Jingya Zhu,^{1,‡} and Pengxuan Zhu³

¹*School of Physics and Electronics,*

Henan University, Kaifeng 475004, China

²*College of Science, University of Shanghai for*

Science and Technology, Shanghai 200093, China

³*ARC Centre of Excellence for Dark Matter Particle Physics,*

University of Adelaide, North Terrace, Adelaide SA 5005, Australia

(Dated: December 31, 2024)

Abstract

To address the longstanding tension between the Constrained Minimal Supersymmetric Standard Model (CMSSM) and recent experimental data, we investigate non-universal gaugino masses within an SU(5) Grand Unified Theory (GUT) framework, focusing on the \tilde{g} -SUGRA scenario where $|M_3| \gg |M_1|, |M_2|$. This hierarchy enables a heavier gluino, thereby evading current experimental bounds on supersymmetric particles. Our analysis reveals that precise Higgs measurements place stringent constraints on the model, requiring $\tan \beta \gtrsim 5$ and $M_0 \gtrsim 20 \tan \beta \text{ GeV}$. Although the \tilde{g} -SUGRA scenario can help reconcile the persistent $(g-2)_\mu$ anomaly, the Higgs constraints significantly restrict its parameter space, making a large contribution to $(g-2)_\mu$ challenging. We also assess the discovery prospects in upcoming dark matter direct detection experiments, including PandaX-xT (200 t.y.), LZ (projected), and XENONnT (20 t.y.), which may not fully cover the viable parameter space. In contrast, future collider experiments—such as the High-Luminosity LHC at 3 ab^{-1} and CLIC₁₅₀₀ at 2.5 ab^{-1} —can comprehensively probe the remaining regions. These findings highlight \tilde{g} -SUGRA as a promising solution to the CMSSM tension and offer clear, testable predictions for upcoming collider searches.

* dongyb@henu.edu.cn

† Corresponding author: kwang@usst.edu.cn

‡ Corresponding author: zhuji@henu.edu.cn

CONTENTS

| | |
|---|----|
| I. Introduction | 2 |
| II. Non-universal gaugino masses in \tilde{g} SUGRA | 4 |
| III. Results and discussion | 7 |
| IV. Conclusions | 22 |
| Acknowledgments | 23 |
| References | 23 |

I. INTRODUCTION

The Standard Model (SM) of particle physics, a foundational framework, has profoundly shaped our understanding of the fundamental constituents and forces of nature. Its robustness was confirmed with the discovery of the Higgs boson at the Large Hadron Collider (LHC) in 2012, a milestone that not only fulfilled a decades-long prediction, but also secured the central role of the SM in modern physics [1, 2]. Subsequent precision measurements of the properties of the Higgs boson have consistently confirmed the predictions of the SM [3, 4]. Despite these successes, the SM has significant limitations. It does not adequately address critical issues such as the hierarchy problem, the anomalous magnetic moment of the muon, and the nature of dark matter, indicating the need for new theoretical developments.

The value of the muon magnetic moment predicted by the SM, a_μ^{SM} , is reported as [5]:

$$a_\mu^{\text{SM}} = 116591810(43) \times 10^{-11}. \quad (1)$$

In 2023, Fermi National Accelerator Laboratory (FNAL) reported new measurement results for the muon magnetic moment [6]:

$$a_\mu^{\text{exp}} = 116592059(22) \times 10^{-11}, \quad (2)$$

which are fully consistent with previous results from both Brookhaven National Laboratory (BNL) and FNAL itself [7, 8]. These data represent a 5σ deviation from the SM predictions,

highlighting a significant challenge to the existing theoretical framework. Further consolidating these findings, the Particle Data Group (PDG) has calculated the world average of the muon anomalous magnetic moment as [9] :

$$\Delta a_\mu \equiv a_\mu^{\text{exp}} - a_\mu^{\text{SM}} = (24.9 \pm 4.8) \times 10^{-10}. \quad (3)$$

In addition, the Planck Collaboration has released its final full-mission measurements of cosmological parameters [10], including the relic density of cold dark matter:

$$\Omega h^2 = 0.1200 \pm 0.0012. \quad (4)$$

These phenomena are difficult to explain within the framework of the SM and strongly suggest the existence of new physics beyond the Standard Model (BSM). To interpret such experimental results, numerous models have been proposed [11–26]. Among these, the low-energy supersymmetric model is one of the most widely discussed extensions of the SM [27–29]. Its primary motivation is to solve the gauge hierarchy problem in a natural way by introducing supersymmetric (SUSY) particles. These particles can also provide additional contributions to the muon g-2 anomaly, providing a potential solution to this puzzle. Moreover, assuming R-parity conservation, the lightest SUSY particle (LSP) is considered a compelling candidate for dark matter [30], capable of explaining the observed relic density in the universe.

The Minimal Supersymmetric Standard Model (MSSM) [31–34] is the simplest supersymmetric extension of the SM, known for its robust ability to explain various experimental anomalies [35–40]. However, it includes over 100 free parameters, making their experimental determination extremely challenging. In contrast, the Constrained MSSM (CMSSM) [41–47] simplifies this by assuming unified values for the gaugino masses, scalar masses and trilinear coupling constants at the Grand Unified Theory (GUT) scale, represented as $M_{1/2}$, M_0 and A_0 respectively. This reduces the number of free parameters to five: M_0 , $M_{1/2}$, A_0 , $\tan\beta$ and the sign of μ . The ratio $\tan\beta$ is defined as V_u/V_d , where V_u and V_d are the Higgs fields that give mass to the up-type quarks and the down-type quarks and leptons, respectively. This approach allows these five parameters to determine all low-energy soft SUSY breaking parameters through the renormalization group equations (RGEs).

The phenomenology of the CMSSM has been extensively studied [48–50]; however, by reducing the number of free parameters, the CMSSM offers a more constrained interpretation

of the experimental data compared to the MSSM. In particular, it struggles to account for the anomalous magnetic moment of the muon while predicting a 125 GeV SM-like Higgs. This challenge arises because the masses of the light electroweakinos, higgsinos, sleptons, and neutrinos, which can contribute significantly to the muon anomalous magnetic moment, are predicted to be heavier than several hundred GeV in the CMSSM under these conditions.

The non-universal gaugino masses within the framework of SU(5) GUT offer a solution to the tensions observed between the CMSSM and current experimental data. Our study focuses on the scenario where $|M_3| \gg |M_1|, |M_2|$, referred to as \tilde{g} SUGRA. We investigate the constraints imposed by current data on this parameter space, consider the annihilation mechanisms of dark matter relevant to this scenario, and explore the detection capabilities of future dark matter experiments. Finally, we evaluate the prospects of future dark matter direct detection experiments and collider studies of SUSY particles to probe this scenario.

This paper is organized as follows. Section II provides a brief overview of the mechanism for generating non-universal gaugino masses in the \tilde{g} SUGRA framework within the context of the SU(5) GUT. Section III presents the numerical results obtained by applying the theoretical and experimental constraints, accompanied by a comprehensive theoretical interpretation. Finally, Section IV provides a summary of our conclusions.

II. NON-UNIVERSAL GAUGINO MASSES IN \tilde{g} SUGRA

Based on different mechanisms of SUSY breaking, the CMSSM can be categorized into three main classes: Gravity Mediated SUSY Breaking (commonly referred to as minimal Supergravity or mSUGRA) [51–55], Anomaly Mediated SUSY Breaking (AMSB) [56–58], and Gauge Mediated SUSY Breaking (GMSB) [59, 60]. Among these, mSUGRA is a highly predictive framework that naturally accommodates a 125 GeV SM-like Higgs boson [61, 62]. In the mSUGRA scenario, the masses of the gauginos (bino, wino, and gluino) are unified at the GUT scale, expressed as $M_1 = M_2 = M_3 = M_{1/2}$.

The GUT of mSUGRA provides a comprehensive framework based on three arbitrary functions: the superpotential, the Kähler potential, and the gauge kinetic function. This framework allows for non-universalities in the soft SUSY-breaking parameters, including scalar masses, gaugino masses, and trilinear couplings [63–68]. In this study, we focus on a scenario where the gaugino masses are non-universal, while other boundary conditions are

maintained at the GUT scale.

The universal boundary conditions for soft parameters can be derived from specific assumptions about the Kähler potential and the gauge kinetic energy function [69]. Generally, the Kähler potential is assumed to be minimal, while the gauge kinetic terms for the vector supermultiplet can be expressed in a general form as:

$$\mathcal{L} \supseteq \int d^2\theta d\tau \left(W^a W^a + a_1 \frac{S}{\Lambda} W^a W^a + b_1 \frac{\Phi_{ab}}{\Lambda} W^a W^b \right), \quad (5)$$

where S and Φ_{ab} represent the singlet and non-singlet chiral superfields of the GUT group, respectively. The field S can develop a vacuum expectation value (VEV) scaled by Λ or lower, while non-singlet Φ_{ab} fields can generate F-term VEV. Soft SUSY-breaking gaugino masses are induced through these terms. Universal gaugino masses are generated by the a_1 term and associated with the $\langle F_S \rangle$, while non-universal gaugino masses are generated by the b_1 term and associated with the $\langle F_{\Phi_{ab}} \rangle$. To obtain non-universal gaugino masses, the non-singlet Higgs field Φ_{ab} must acquire non-vanishing F-term VEV. These operators can also contribute additional non-universalities to other soft SUSY breaking terms, such as trilinear couplings and sfermion masses.

Within the SU(5) GUT framework, the field Φ_{ab} can belong to any of the irreducible representations arising from the symmetric product of the adjoint representations. Specifically, the symmetric product of two adjoint representations, $\mathbf{24} \otimes \mathbf{24}$, can be decomposed into the following irreducible representations of SU(5):

$$(\mathbf{24} \otimes \mathbf{24})_{\text{symm}} = \mathbf{1} \oplus \mathbf{24} \oplus \mathbf{75} \oplus \mathbf{200}. \quad (6)$$

Here, $\mathbf{24}$, $\mathbf{75}$, and $\mathbf{200}$ represent the chiral supermultiplets of SU(5). When Φ_{ab} is a singlet, as assumed in mSUGRA, the gaugino masses acquire a uniform value at the GUT scale. In contrast, if Φ_{ab} is a non-singlet belonging to a higher-dimensional representation of SU(5), the gaugino masses become non-uniform but remain interrelated through the representation invariants. For a representation denoted as \mathbf{n} , the three gaugino masses at the GUT scale possess distinct coefficients relative to the SUSY breaking mass parameter, and take the following form:

$$M_{1,2,3} = C_{1,2,3}^{\mathbf{n}} M_{1/2}^{\mathbf{n}}, \quad (7)$$

where $M_{1/2}^{\mathbf{n}}$ is the soft gaugino mass arising from the F-term VEV in the representation \mathbf{n} .

The coefficients $C_{1,2,3}^n$ for specific representations are given as:

$$\begin{aligned}
C_{1,2,3}^1 &= (1, 1, 1), \\
C_{1,2,3}^{24} &= (-1, -3, 2), \\
C_{1,2,3}^{75} &= (-5, 3, 1), \\
C_{1,2,3}^{200} &= (10, 2, 1).
\end{aligned} \tag{8}$$

For the Higgs fields belonging to the SU(5) GUT group with representations **24**, **75**, and **200**, along with a gauge singlet S , the Lagrangian can be expressed as:

$$\mathcal{L} = \int d^2\theta \left(\frac{\theta\tau}{4} W^a W^b \right) \frac{1}{\Lambda} [c_0 S \delta_{ab} + c_1 (\Phi^{24})_{ab} + c_2 (\Phi^{75})_{ab} + c_3 (\Phi^{200})_{ab}]. \tag{9}$$

In particular, it is theoretically possible for the Higgs fields in these high-dimensional representations to acquire only the lowest component VEVs, while the singlet S can acquire both its lowest component VEV and the F-term VEV. This configuration ensures the preservation of the SU(3) $_C$ \times SU(2) $_L$ \times U(1) $_Y$ gauge symmetry, corresponding to the gauge boson superpartners, gluino (\tilde{g}), the wino (\tilde{W}), and the bino (\tilde{B}), respectively.

The VEVs of the Higgs fields Φ^{24} , Φ^{75} and Φ^{200} can be expressed in their respective adjoint representations, corresponding to 5×5 , 10×10 , and 15×15 matrices. These matrices take on the following specific forms:

$$\begin{aligned}
\langle \Phi^{24} \rangle &= v_U \sqrt{\frac{3}{5}} \text{diag} \left(-\frac{1}{3}, -\frac{1}{3}, -\frac{1}{3}, \frac{1}{2}, \frac{1}{2} \right), \\
\langle \Phi^{75} \rangle &= \frac{v_U}{2\sqrt{3}} \text{diag} \left(\underbrace{1, \dots, 1}_3, \underbrace{-1, \dots, -1}_6, 3 \right), \\
\langle \Phi^{200} \rangle &= \frac{v_U}{2\sqrt{3}} \text{diag} \left(\underbrace{1, \dots, 1}_6, \underbrace{-2, \dots, -2}_6, \underbrace{2, \dots, 2}_3 \right),
\end{aligned} \tag{10}$$

where v_U denotes the GUT breaking scale, which is assumed to have a universal value for all Higgs fields. In the most general scenarios, the singlet S and the high-dimensional representations of Higgs fields are assumed to acquire universal F-term VEVs, F_Λ , under the assumption of trivial kinetic terms. Then M_1 , M_2 , and M_3 can get contributions from S , Φ^{24} , Φ^{75} and Φ^{200} at GUT scale and the ratio of gauginos is given by:

$$M_1 : M_2 : M_3 = \left[c_0 - \frac{c_1}{4\sqrt{15}} + \frac{5c_2}{4\sqrt{3}} + \frac{5c_3}{2\sqrt{3}} \right] : \left[c_0 - \frac{3c_1}{4\sqrt{15}} - \frac{3c_2}{4\sqrt{3}} + \frac{c_3}{2\sqrt{3}} \right] : \left[c_0 + \frac{c_1}{2\sqrt{15}} - \frac{c_2}{4\sqrt{3}} + \frac{c_3}{4\sqrt{3}} \right]. \quad (11)$$

Thus, an arbitrary ratio of $M_1 : M_2 : M_3$ at the GUT scale can be achieved by appropriately tuning the coefficients. A particularly interesting scenario arises when $M_3 \gg M_1, M_2$, ensuring that the radiative break of the electroweak symmetry is primarily driven by the gluino. This framework, often referred to as \tilde{g} -SUGRA [70], leads to rich phenomenological implications. In this case, the gluino significantly affects the RGEs of the squarks, contributing to their masses as the RGEs run from the GUT scale to the electroweak scale. Conversely, at the one-loop level, the gluino does not enter the RGEs of sleptons, leaving their masses unaffected. Such a scenario predicts heavy squarks, allowing them to escape current experimental constraints on squark masses. At the same time, the presence of relatively light sleptons can lead to a number of interesting phenomenological consequences.

III. RESULTS AND DISCUSSION

We use the `SuSpect-2.52` [71] package to implement the theoretical and experimental constraints in our analysis, assuming $\text{sign}(\mu) = +1$. The remaining parameters are selected within the following ranges:

$$\begin{aligned} M_0, |M_1|, |M_2| &< 1 \text{ TeV}, \\ 1 \text{ TeV} &< |M_3| < 10 \text{ TeV}, \\ |A_0| &< 10 \text{ TeV}, \\ 1 &< \tan\beta < 50. \end{aligned} \quad (12)$$

The following constraints are considered in our analysis:

- (1) The lightest CP-even Higgs boson is assumed to be the SM-like Higgs boson, with a mass of 125 ± 2 GeV [72–75].
- (2) The constraints on the squark and gluino masses are derived from the latest results of the LHC searches [76]:

$$m_{\tilde{g}} > 2 \text{ TeV}, \quad m_{\tilde{t}} > 0.7 \text{ TeV}, \quad m_{\tilde{q}_{1,2}} > 2 \text{ TeV}, \quad (13)$$

while the chargino and slepton mass constraints are derived from LEP results [77]:

$$m_{\tilde{\tau}} > 93.2 \text{ GeV}, \quad m_{\tilde{\chi}^{\pm}} > 103.5 \text{ GeV}. \quad (14)$$

- (3) Direct searches for low-mass and high-mass resonances have been conducted at LEP, Tevatron, and LHC. These constraints are implemented in our analysis using the HiggsSignal-2.6.0 [78] and HiggsBounds-5.10.0 [79] packages.
- (4) The dark matter relic density constraints are derived from the Planck observations [10], while the direct search results for dark matter are based on the 2022 findings of the LUX-ZEPLIN (LZ) experiment [80]. The relic density and the dark matter annihilation cross-section are calculated using the micrOMEGAs-5.3.41 package [81, 82]. Since the relic density may also include contributions from other dark matter species, only the upper bound is applied in this analysis, given as $0 < \Omega h^2 < 0.12$.
- (5) The constraints from B physics, such as $B \rightarrow s\gamma$, $B_s \rightarrow \mu^+\mu^-$, and $B^+ \rightarrow \tau^+\nu$ are adopted based on the latest results provided by the PDG 2024 [9]:

$$\begin{aligned} Br(B \rightarrow s\gamma) &= (3.49 \pm 0.38) \times 10^{-4}, \\ Br(B^+ \rightarrow \tau^+\nu) &= (1.09 \pm 0.48) \times 10^{-4}, \\ Br(B_s \rightarrow \mu^+\mu^-) &= (3.01 \pm 0.87) \times 10^{-9}. \end{aligned} \quad (15)$$

- (6) The constraints on the muon anomalous magnetic moment (Δa_μ), defined as the difference between the experimental measurement and the SM prediction, are characterized by the following features [6, 9]

$$\Delta a_\mu \equiv a_\mu^{\text{exp}} - a_\mu^{\text{SM}} = (24.9 \pm 4.8) \times 10^{-10}. \quad (16)$$

The muon anomalous magnetic moment is calculated at the two-loop level using the GM2Calc-2.1.0 package [83, 84].

- (7) The constraints from direct searches for supersymmetric particles at LEP, Tevatron, and LHC are incorporated into the analysis. The SModelS-3.0.0 package [85–87] is used to calculate the expected signal strength r , which is used to evaluate the consistency of the model with experimental results.

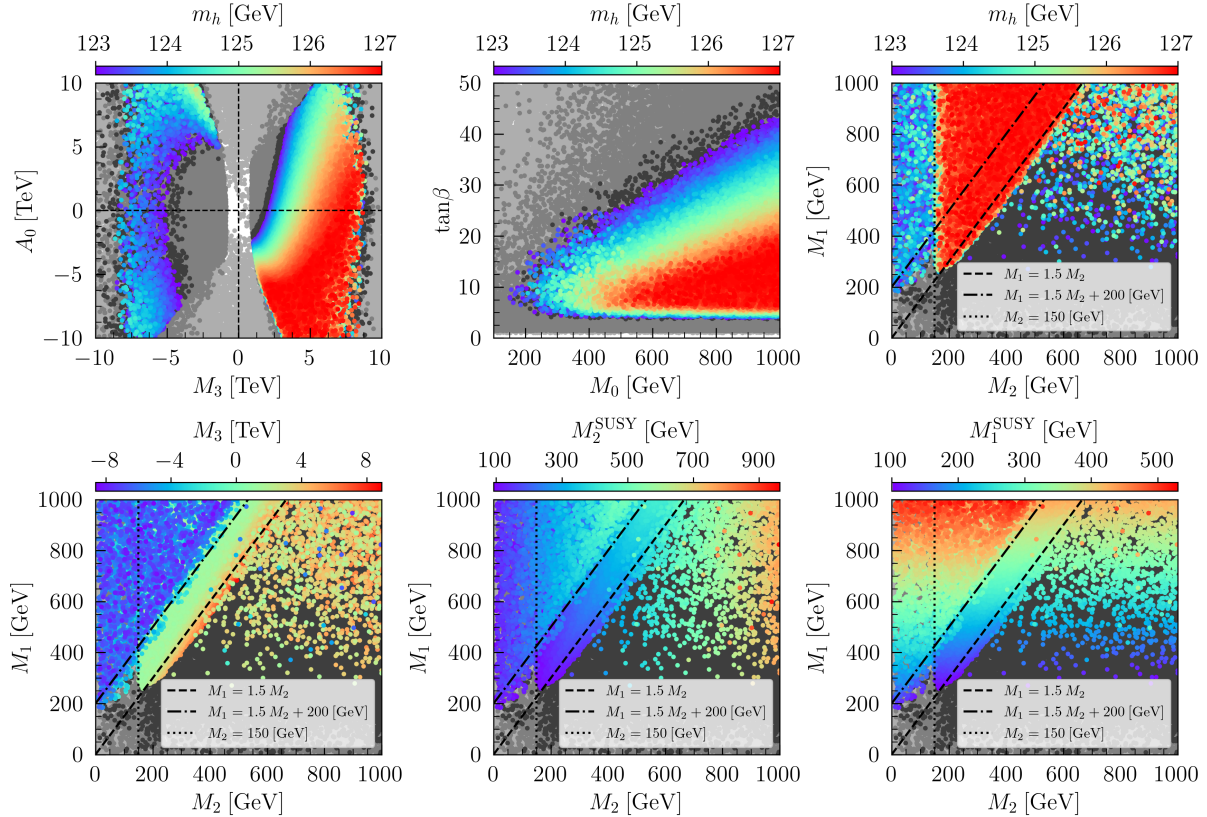


FIG. 1. Surviving samples in the A_0 versus M_3 plane (upper left), the $\tan\beta$ versus M_0 plane (upper middle), and the M_1 versus M_2 plane (upper right and lower three), with colors indicating the SM-like Higgs mass m_h (upper three), the value of input parameter M_3 (lower left), the value of M_2 at the soft SUSY scale (lower middle), and the value of M_1 at the soft SUSY scale (lower right), respectively. The light gray samples are excluded by theoretical constraint, the gray samples are excluded that cannot give a suitable SM-like Higgs mass, and the black samples are excluded by the dark matter data. The samples with a larger value of m_h are projected on top of smaller ones (upper panels) and the samples with a smaller value of M_3 are projected on top of larger ones (lower panels).

In Fig. 1, we present all surviving samples in the A_0 versus M_3 plane (upper left), the $\tan\beta$ versus M_0 plane (upper middle), and the M_1 versus M_2 plane (upper right and lower three), respectively. Their colors indicate the SM-like Higgs mass m_h (upper three), the value of input parameter M_3 (lower left), the value of M_2 at the soft SUSY scale (lower middle), and the value of M_1 at the soft SUSY scale (lower right), respectively. The light gray samples are excluded by the theoretical constraints, the gray samples are excluded that

cannot give a suitable SM-like Higgs mass, and the black samples are excluded by the dark matter data. The samples with a larger value of m_h are projected on top of smaller ones (upper panels), and the samples with a smaller value of M_3 are projected on top of larger ones (lower panels). Several conclusions can be drawn from these figures:

- The primary constraints on M_3 , A_0 , M_0 and $\tan\beta$ arise from theoretical considerations and Higgs data. In contrast, the primary constraints on M_1 and M_2 are imposed by dark matter data. The reasons for these differences will be discussed in more detail later.
- In the upper right and lower three panels of Fig. 1, the surviving samples in the M_1 versus M_2 plane can be broadly classified into three categories:
 - **Class A:** $M_3 > 0$ GeV, $M_1/M_2 \gtrsim 1.5$.
 - **Class B:** $M_3 > 0$ GeV, $M_1/M_2 \lesssim 1.5$.
 - **Class C:** $M_3 < 0$ GeV, $M_1 \gtrsim 1.5M_2 + 200$ GeV.

In Fig. 2, surviving samples are shown in the A_0 versus M_0 planes (upper three), the $\tan\beta$ versus M_0 planes (lower left and lower middle), and the $\tan\beta$ versus m_A plane (lower right), with colors indicating the higgsino mass parameter μ (upper left), the pseudoscalar particle Higgs mass m_A (upper middle), the SUSY contributions to muon g-2 Δa_μ (upper right and lower middle), the lighter smuon mass $m_{\tilde{\mu}_1}$ (lower left), the branching ratio of $B_s \rightarrow \mu^+ \mu^-$ ($\text{Br}(B_s \rightarrow \mu^+ \mu^-)$) (lower right), respectively. Meanwhile, samples with larger values of colors are projected on top of smaller ones for the upper right and lower three panels. By combining Fig. 1 and Fig. 2, the following conclusions can be drawn:

- From the upper panels of Fig. 1, it is evident that Higgs data impose a strong constraint on the parameter space. Specifically, the data requires $\tan\beta \gtrsim 5$ and $M_0 \gtrsim 20 \tan\beta$ GeV. In addition, a negative M_3 is favor to predict a light Higgs mass, whereas a positive M_3 is favor to predict a heavy Higgs mass.
- From the lower left panel of Fig. 1, it can be observed that samples with negative M_3 can only surviving in **Class C**. In other words, to obtain a negative value of M_3 requires $M_1 \gtrsim 1.5M_2 + 200$ GeV. In contrast, the samples with positive M_3 only need $M_2 \gtrsim 200$ GeV.

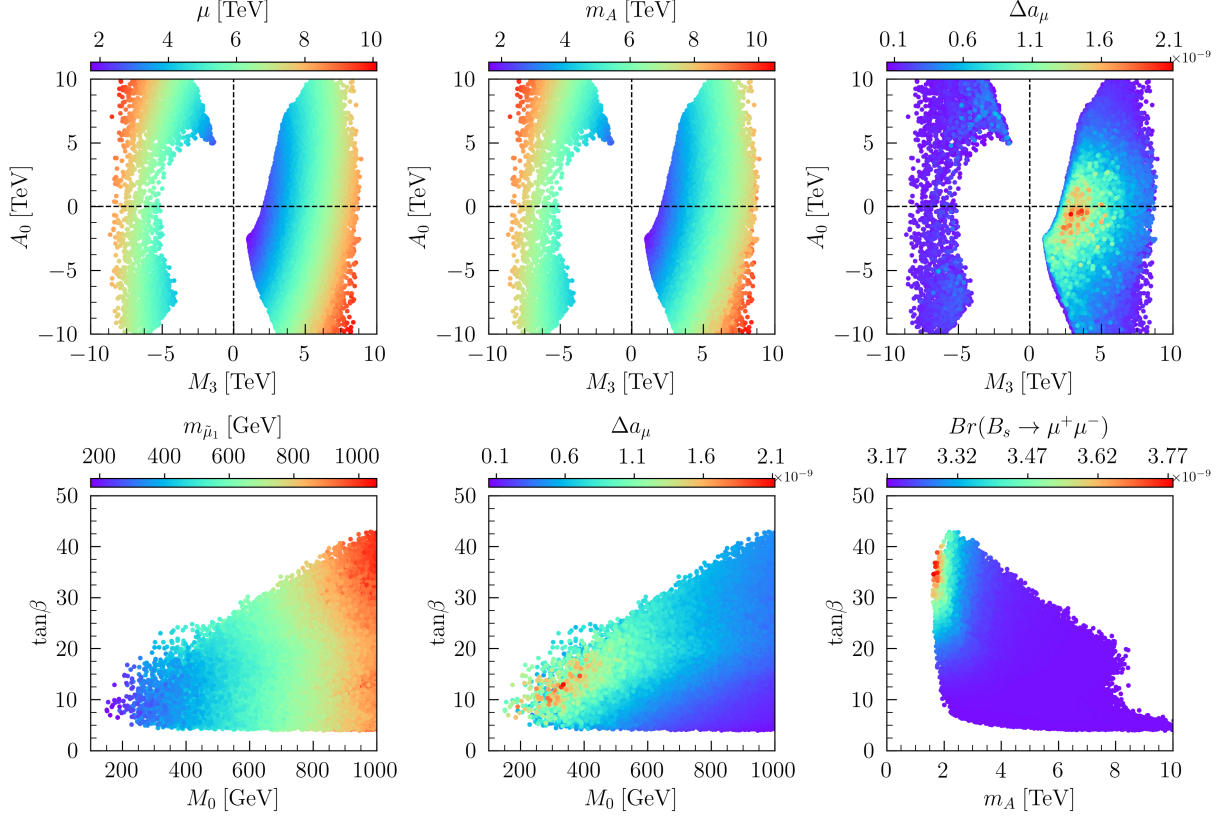


FIG. 2. Surviving samples in the A_0 versus M_0 planes (upper three), the $\tan\beta$ versus M_0 planes (lower left and lower middle), and the $\tan\beta$ versus m_A plane (lower right), with colors indicating the higgsino mass parameter μ (upper left), the pseudoscalar Higgs mass m_A (upper middle), the SUSY contributions to muon g-2 Δa_μ (upper right and lower middle), the lighter smuon mass $m_{\tilde{\mu}_1}$ (lower left), the branching ratio of $B_s \rightarrow \mu^+ \mu^-$ ($Br(B_s \rightarrow \mu^+ \mu^-)$) (lower right), respectively. For the upper right and lower three panels, the samples with larger values of colors are projected on top of smaller ones.

- From the lower middle and right panels of Fig. 1, it can be observed that, for the same M_1 (M_2) at the GUT scale, the samples in **Class C** result in larger M_1 (M_2) values at the soft SUSY scale compared to samples in other classes after RGEs running. This is because a negative M_3 provides a positive contribution to M_1 (M_2) during the RGEs evolution, whereas a positive M_3 leads to a negative contribution. These results are consistent with Eqs.(38) and (39) in the Appendix A in Ref. [26].
- From the upper right panel of Fig. 1, it can be observed that samples in **Class A**

tend to predict a heavier SM-like Higgs. Furthermore, a heavy SM-like Higgs is also favored by moderate values of $\tan\beta$ (around 10) and relatively large M_0 (larger than 400 GeV), as shown in the upper middle panel of Fig. 1.

- By combining the upper left and middle panels of Fig. 2, it can be observed that the Higgsino mass μ is nearly equal to the pseudoscalar Higgs mass m_A , and both are directly proportional to M_3 . This relationship arises because, in supersymmetric models, the parameter μ takes the form:

$$\mu^2 = \frac{M_{H_d}^2 - M_{H_u}^2 \tan^2 \beta}{\tan^2 \beta - 1} - \frac{m_Z^2}{2}. \quad (17)$$

Since $\tan\beta \gg 1$, we have $\tan^2 \beta - 1 \approx \tan^2 \beta$ and $|M_{H_u}| \gg |M_{H_d}|$. Under these approximations, the term $M_{H_d}^2 - M_{H_u}^2 \tan^2 \beta$ reduces to $M_{H_u}^2 \tan^2 \beta$, and the first term in Eq. (17) simplifies to approximately $M_{H_u}^2$. Furthermore, since $|M_{H_u}| \gg |m_Z|$, it follows that $\mu \approx M_{H_u}$. At the same time, the pseudoscalar Higgs mass parameter m_A is given by:

$$m_A^2 = \frac{\tan^2 \beta + 1}{\tan^2 \beta - 1} (M_{H_d}^2 - M_{H_u}^2) - m_Z^2. \quad (18)$$

With $\tan\beta \gg 1$ and $|M_{H_u}| \gg |M_{H_d}|$, one can find that $\tan^2 \beta - 1 \approx \tan^2 \beta + 1$ and $M_{H_d}^2 - M_{H_u}^2 \approx M_{H_u}^2$. This leads to $m_A \approx M_{H_u} \approx \mu$. According to the Eqs.(59) in the Appendix A in Ref. [26], M_{H_u} is nearly directly proportional to M_3 . Consequently, both μ and m_A are approximately directly proportional to M_3 .

- By combining the upper right and lower middle panels of Fig. 2, it appears that small values of $|A_0|$, M_3 , and M_0 tend to provide a larger contribution to Δa_μ . In particular, a sample with $M_0 \sim 250$ GeV, $|A_0| \lesssim -1$ TeV, $M_3 \sim 4$ TeV, and $\tan\beta \sim 10$ yields a sizable contribution to Δa_μ ($\sim 2.1 \times 10^{-9}$). In SUSY, the primary contribution to Δa_μ comes from smuon interactions and is given by [88, 89]:

$$a_\mu^{\tilde{\mu}} \approx a_0 \frac{1 + \delta^{2\text{-loop}}}{1 + \Delta_\mu} \left(\frac{\tan\beta \cdot (100 \text{ GeV})^2}{m_{\tilde{\mu}_L}^2 m_{\tilde{\mu}_R}^2 / (M_1 \mu)} \right) \left(\frac{f_N}{1/6} \right), \quad (19)$$

where $a_0 = 1.5 \times 10^{-10}$. This expression shows that the smuon contribution is proportional to $\tan\beta$ and inversely proportional to $m_{\tilde{\mu}}^4$. Therefore, achieving a significant supersymmetric contribution to $g-2$ requires light sleptons and large $\tan\beta$. Smaller M_0 values can produce lighter smuons, as seen in the lower left panel of Fig. 2. However,

scenarios with small M_0 and large $\tan\beta$ encounter significant theoretical constraints, including issues with RGEs due to the presence of non-perturbative effects or Landau poles. Additionally, these scenarios are also constrained by Higgs data, as they struggle to produce an SM-like Higgs with a mass of 125 GeV. Consequently, achieving an extremely large contribution to $g - 2$ in this framework is highly challenging.

- From the lower right panel of Fig. 2, it can be observed that a lighter m_A (~ 2 TeV) and a larger $\tan\beta$ (~ 35) result in a higher branching ratio for $B_s \rightarrow \mu^+\mu^-$. This behavior can be explained within SUSY models, where the branching ratio of $B_s \rightarrow \mu^+\mu^-$ is given by:

$$\text{Br}(B_s \rightarrow \mu^+\mu^-) \propto \frac{m_t^4 \mu^2 A_t^2 \tan^6 \beta}{m_A^4 m_t^4}. \quad (20)$$

From this expression, it is evident that $\text{Br}(B_s \rightarrow \mu^+\mu^-)$ is directly proportional to $\tan^6 \beta$ and inversely proportional to m_A^4 . This explains why a larger $\tan\beta$ and a smaller m_A enhance the branching ratio.

In Fig. 3, to understand the dark matter annihilation mechanisms of the surviving samples, we project them onto the M_1 versus M_2 planes (upper three and lower left), the lightest neutralino mass $m_{\tilde{\chi}_1^0}$ versus the lighter stau mass $m_{\tilde{\tau}_1}$ plane (lower middle), and the lightest neutralino mass $m_{\tilde{\chi}_1^0}$ versus the lightest chargino mass $m_{\tilde{\chi}_1^\pm}$ plane (lower right). The colors indicate the lightest neutralino mass $m_{\tilde{\chi}_1^0}$ (upper left), the bino component of the lightest neutralino (upper middle), the wino component of the lightest neutralino (upper right), and the dark matter relic density Ωh^2 (lower three), respectively. Meanwhile, samples with smaller values of M_3 are projected on top of larger ones for the upper left panels, and the samples with larger values of $|N_{11}|^2$ are projected on top of smaller ones for the upper middle panel, the samples with a smaller value of $|N_{12}|^2$ are projected on top of larger ones for the upper right panel, and the samples with larger value of Ωh^2 are projected on top of smaller ones for the lower three panels. The following conclusions can be drawn:

- From the upper left panel of Fig. 3, it is evident that the lightest neutralino mass $m_{\tilde{\chi}_1^0}$ is nearly proportional to M_2 in **Class A** and **Class C**, while it is nearly proportional to M_1 in **Class B**. This behavior suggests the dominant component of the lightest neutralino $\tilde{\chi}_1^0$, as M_1 and M_2 are the mass parameters associated with the bino and wino, respectively. Furthermore, samples in **Class C** predict a heavier $\tilde{\chi}_1^0$ compared

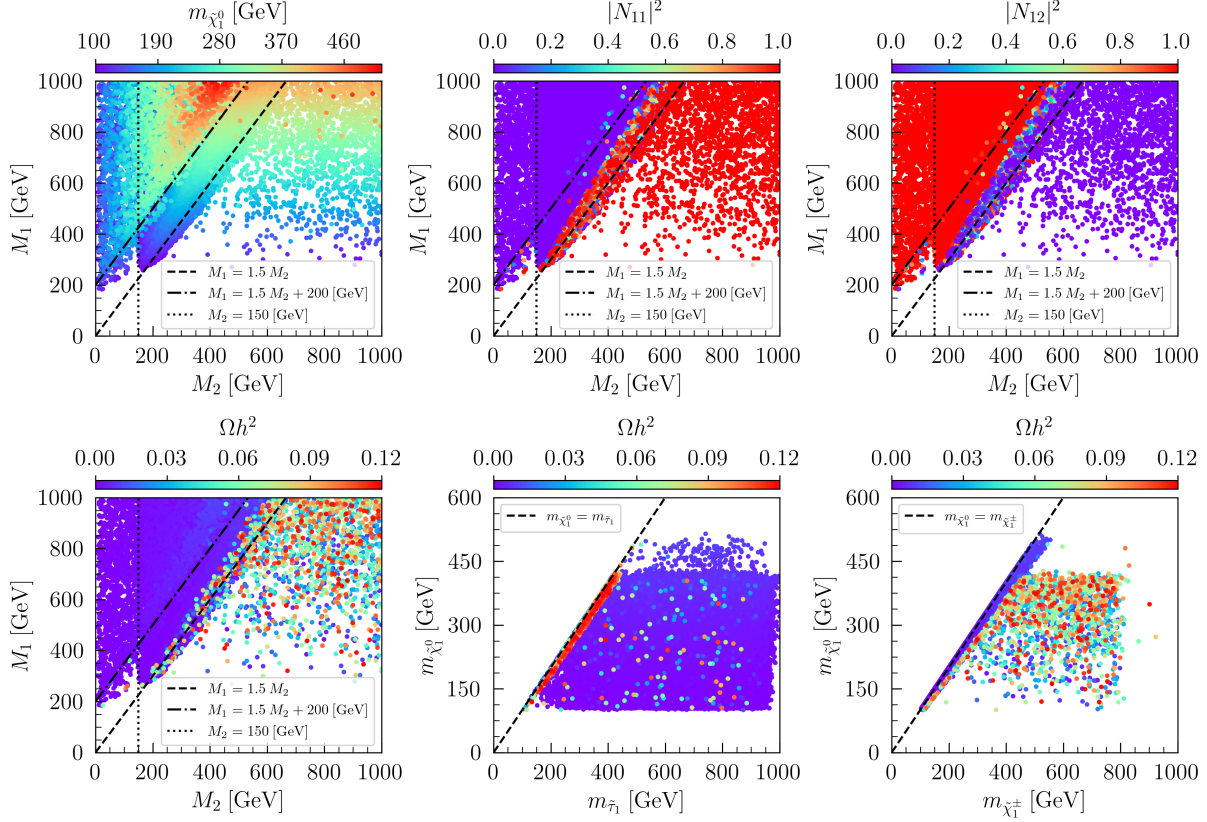


FIG. 3. Surviving samples in the M_1 versus M_2 planes (upper three and lower left), the lightest neutralino mass $m_{\tilde{\chi}_1^0}$ versus lighter stau mass $m_{\tilde{\tau}_1}$ plane (lower middle), and the lightest neutralino mass $m_{\tilde{\chi}_1^0}$ versus the lightest chargino mass $m_{\tilde{\chi}_1^\pm}$ plane (lower right), with colors indicating the lightest neutralino mass $m_{\tilde{\chi}_1^0}$ (upper left), the bino component in lightest neutralino (upper middle), the wino component in lightest neutralino (upper right), and the dark matter relic density Ωh^2 (lower three), respectively. The samples with smaller values of M_3 are projected on top of larger ones for the upper left panels, the samples with larger values of $|N_{11}|^2$ are projected on top of smaller ones for the upper middle panel, the samples with smaller value of $|N_{12}|^2$ are projected on top of larger ones for the upper right panel, and the samples with larger value of Ωh^2 are projected on top of smaller ones for the lower three panels.

to those in **Class A** for the same M_2 . This is attributed to the additional contribution of M_3 to M_2 at the soft SUSY scale.

- From the upper middle and right panels of Fig. 3, it can be observed that the lightest neutralino $\tilde{\chi}_1^0$ is predominantly wino-like in **Class A** and **Class C**, while it is predom-

inantly bino-like in **Class B**. Additionally, $\tilde{\chi}_1^0$ typically does not exhibit wino-bino mixing, except for samples near the lower edge of **Class A** and **Class B**.

- By combining the upper middle, upper right, and lower left panels of Fig. 3, it becomes clear that a larger dark matter relic density Ωh^2 is only achieved when $\tilde{\chi}_1^0$ is predominantly bino-like. However, the Ωh^2 predicted for bino-like $\tilde{\chi}_1^0$ is often excessively large and strongly constrained by experimental dark matter data. This limitation explains the scarcity of surviving samples in **Class B**. In contrast, when $\tilde{\chi}_1^0$ exhibits wino-bino mixing, a significantly smaller Ωh^2 can be achieved, although it remains larger than in scenarios where $\tilde{\chi}_1^0$ is predominantly wino-like.
- From the lower left and middle panels of Fig. 3, it can be observed that the mass of $\tilde{\chi}_1^0$ ($m_{\tilde{\chi}_1^0}$) and the mass of the lighter smuon $m_{\tilde{\tau}_1}$ are nearly degenerate when $\tilde{\chi}_1^0$ is bino-like. In contrast, $m_{\tilde{\tau}_1}$ becomes significantly larger than $m_{\tilde{\chi}_1^0}$ when $\tilde{\chi}_1^0$ is wino-like. This behavior provides insight into the annihilation mechanisms of $\tilde{\chi}_1^0$. When $\tilde{\chi}_1^0$ is bino-like, its annihilation is primarily mediated by interactions with $\tilde{\tau}_1$. Since $\tilde{\tau}_1$ is only slightly heavier than $\tilde{\chi}_1^0$, the annihilation process occurs relatively slowly, allowing for the accumulation of a sufficient relic density.
- From the lower left and right panels of Fig. 3, it can be observed that if $\tilde{\chi}_1^0$ is wino-like, its mass is nearly degenerate with the mass of the lightest chargino ($m_{\tilde{\chi}_1^\pm}$), which aligns with theoretical expectations. Consequently, $\tilde{\chi}_1^0$ can consistently co-annihilate with $\tilde{\chi}_1^\pm$ in wino-like scenarios. However, due to the high annihilation rate associated with this co-annihilation process, it is unable to produce a sufficient relic density (Ωh^2). In contrast, if $\tilde{\chi}_1^0$ is bino-like, the mass of $\tilde{\chi}_1^\pm$ is significantly larger than that of $\tilde{\chi}_1^0$, making co-annihilation between the two particles inefficient.

After examining the annihilation mechanisms of $\tilde{\chi}_1^0$ for the surviving samples, we identify the following primary mechanisms. The main Feynman diagrams illustrating these dominant annihilation mechanisms are shown in Fig. 4.

- Stau annihilation : $\tilde{\tau}_1^+ \tilde{\tau}_1^- \rightarrow hh, W^+W^-, t\bar{t}, \tilde{\tau}_1^+ \tilde{\tau}_1^- \rightarrow \tau^+ \tau^-$.
- Neutralino-stau coannihilation : $\tilde{\chi}_1^0 \tilde{\tau}_1^\pm \rightarrow \tau^\pm h/A$.
- Neutralino annihilation : $\tilde{\chi}_1^0 \tilde{\chi}_{1,2}^0 \rightarrow W^+W^-$.

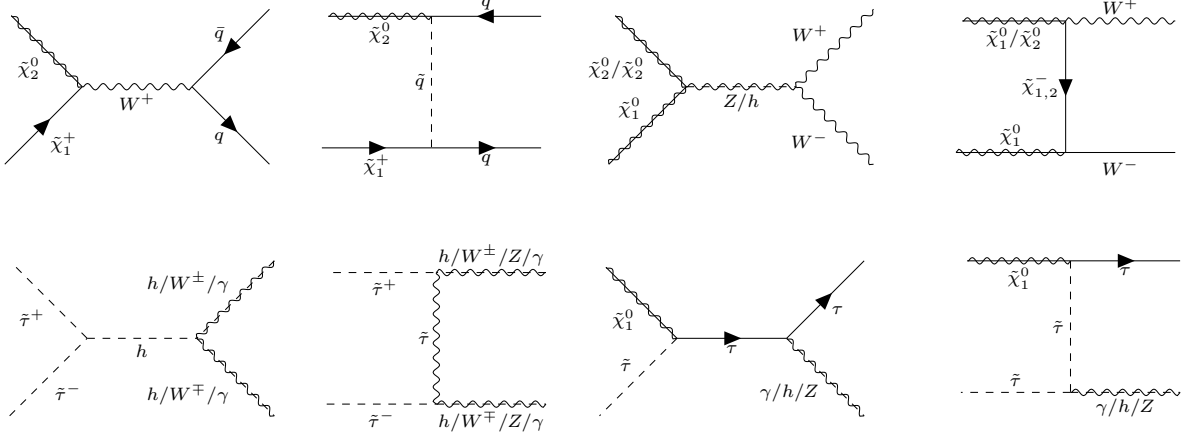


FIG. 4. Main Feynman diagrams illustrating $\tilde{\chi}_1^\pm$ coannihilation (upper panels) and $\tilde{\tau}, \tilde{\chi}_1^0$ hybrid annihilation (lower panels).

- Neutralino-chargeino coannihilation : $\tilde{\chi}_{1,2}^0 \tilde{\chi}_1^\pm \rightarrow u\bar{d}, c\bar{s}, t\bar{b}$.
- Chargeino annihilation : $\tilde{\chi}_1^+ \tilde{\chi}_1^- \rightarrow W^+ W^-$.

The surviving samples can be categorized into four classes based on their dominant annihilation mechanisms:

$$\begin{aligned}
\tilde{\tau} \tilde{\chi}_1^0 \text{ coannihilation} &: \frac{m_{\tilde{\tau}_1}}{m_{\tilde{\chi}_1^0}} < 1.1. \\
\tilde{\chi}_1^0 \tilde{\chi}_1^\pm \text{ coannihilation} &: \frac{m_{\tilde{\tau}_1}}{m_{\tilde{\chi}_1^0}} \gtrsim 1.1, \quad 1 < \frac{m_{\tilde{\chi}_1^\pm}}{m_{\tilde{\chi}_1^0}} \lesssim 1.05. \\
\tilde{\chi}_1^\pm \tilde{\chi}_1^0 \text{ coannihilation} &: \frac{m_{\tilde{\tau}_1}}{m_{\tilde{\chi}_1^0}} \gtrsim 1.1, \quad 1.05 \lesssim \frac{m_{\tilde{\chi}_1^\pm}}{m_{\tilde{\chi}_1^0}} < 1.1. \\
\tilde{\chi}_1^0 \text{ annihilation} &: \frac{m_{\tilde{\tau}_1}}{m_{\tilde{\chi}_1^0}} \gtrsim 1.1, \quad \frac{m_{\tilde{\chi}_1^\pm}}{m_{\tilde{\chi}_1^0}} \approx 1.1.
\end{aligned} \tag{21}$$

The dominant annihilation channels for each coannihilation scenario are as follows:

- For $\tilde{\tau} \tilde{\chi}_1^0$ coannihilation, the primary channels are stau annihilation and neutralino-stau coannihilation.
- For $\tilde{\chi}_1^0 \tilde{\chi}_1^\pm$ coannihilation, the major channels are neutralino-chargeino coannihilation and neutralino annihilation.
- For $\tilde{\chi}_1^\pm \tilde{\chi}_1^0$ coannihilation, the main channels are chargeino annihilation and neutralino-chargeino coannihilation.

TABLE I. The top 10 annihilation channels and their relative contributions to σv for the four benchmark points.

| P1 | P2 | P3 | P4 |
|--|--|--|---|
| $\tilde{\chi}_1^+ \tilde{\chi}_2^0 \rightarrow u\bar{d}, 0.08$ | $\tilde{\tau}_1^+ \tilde{\tau}_1^- \rightarrow hh, 0.17$ | $\tilde{\chi}_1^0 \tilde{\chi}_1^0 \rightarrow W^+W^-, 0.18$ | $\tilde{\chi}_1^0 \tilde{\tau}_1^- \rightarrow \gamma\tau, 0.23$ |
| $\tilde{\chi}_1^+ \tilde{\chi}_2^0 \rightarrow c\bar{s}, 0.08$ | $\tilde{\tau}_1^+ \tilde{\tau}_1^- \rightarrow W^+W^-, 0.16$ | $\tilde{\chi}_1^0 \tilde{\chi}_2^0 \rightarrow W^+W^-, 0.12$ | $\tilde{\tau}_1^+ \tilde{\tau}_1^- \rightarrow \tau^+\tau^-, 0.21$ |
| $\tilde{\chi}_1^+ \tilde{\chi}_2^0 \rightarrow t\bar{b}, 0.07$ | $\tilde{\chi}_1^0 \tilde{\tau}_1^\pm \rightarrow h\tau^\pm, 0.12$ | $\tilde{\chi}_1^+ \tilde{\chi}_1^0 \rightarrow u\bar{d}, 0.07$ | $\tilde{\chi}_1^0 \tilde{\tau}_1^\pm \rightarrow Z\tau^\pm, 0.09$ |
| $\tilde{\chi}_2^0 \tilde{\chi}_2^0 \rightarrow W^+W^-, 0.07$ | $\tilde{\tau}_1^+ \tilde{\tau}_1^- \rightarrow t\bar{t}, 0.11$ | $\tilde{\chi}_1^+ \tilde{\chi}_1^0 \rightarrow c\bar{s}, 0.07$ | $\tilde{\chi}_1^0 \tilde{\chi}_1^+ \rightarrow \tau h, 0.08$ |
| $\tilde{\chi}_1^0 \tilde{\chi}_2^0 \rightarrow W^+W^-, 0.07$ | $\tilde{\chi}_1^0 \tilde{\tau}_1^\pm \rightarrow \gamma\tau^\pm, 0.10$ | $\tilde{\chi}_2^0 \tilde{\chi}_2^0 \rightarrow W^+W^-, 0.06$ | $\tilde{\tau}_1^+ \tilde{\tau}_1^- \rightarrow hh, 0.07$ |
| $\tilde{\chi}_1^0 \tilde{\chi}_2^0 \rightarrow ZW^+, 0.06$ | $\tilde{\tau}_1^+ \tilde{\tau}_1^- \rightarrow ZZ, 0.08$ | $\tilde{\chi}_1^+ \tilde{\chi}_2^0 \rightarrow u\bar{d}, 0.06$ | $\tilde{\tau}_1^+ \tilde{\tau}_1^- \rightarrow W^+W^-, 0.06$ |
| $\tilde{\chi}_1^+ \tilde{\chi}_1^+ \rightarrow W^+W^+, 0.05$ | $\tilde{\tau}_1^+ \tilde{\tau}_1^- \rightarrow \tau^+\tau^-, 0.08$ | $\tilde{\chi}_1^+ \tilde{\chi}_2^0 \rightarrow c\bar{s}, 0.06$ | $\tilde{\tau}_1^+ \tilde{\tau}_1^- \rightarrow \gamma\gamma, 0.06$ |
| $\tilde{\chi}_1^+ \tilde{\chi}_1^0 \rightarrow u\bar{d}, 0.04$ | $\tilde{\chi}_1^0 \tilde{\tau}_1^\pm \rightarrow Z\tau^\pm, 0.06$ | $\tilde{\chi}_1^+ \tilde{\chi}_1^0 \rightarrow t\bar{b}, 0.05$ | $\tilde{\tau}_1^+ \tilde{\tau}_1^- \rightarrow t\bar{t}, 0.05$ |
| $\tilde{\chi}_1^+ \tilde{\chi}_1^0 \rightarrow c\bar{s}, 0.04$ | $\tilde{\chi}_1^0 \tilde{\tau}_1^\pm \rightarrow W^\pm\nu_\tau, 0.06$ | $\tilde{\chi}_1^+ \tilde{\chi}_2^0 \rightarrow t\bar{b}, 0.04$ | $\tilde{\chi}_1^0 \tilde{\tau}_1^\pm \rightarrow W^\pm\nu_\tau, 0.04$ |
| $\tilde{\chi}_1^0 \tilde{\chi}_1^0 \rightarrow W^+W^-, 0.04$ | $\tilde{\tau}_1^+ \tilde{\tau}_1^- \rightarrow \gamma\gamma, 0.03$ | $\tilde{\chi}_1^+ \tilde{\chi}_2^0 \rightarrow ZW^+, 0.03$ | $\tilde{\tau}_1^+ \tilde{\tau}_1^- \rightarrow ZZ, 0.03$ |

- For $\tilde{\chi}_1^0$ annihilation, the dominant channel is neutralino annihilation.

We provide detailed annihilation information for four benchmark points, including their top 10 annihilation channels and the relative contributions to σv , in Table I. Additional information about these benchmark points is summarized in Table II.

In Fig. 5, surviving samples are shown in the M_1 versus M_2 plane (left), the lightest neutralino mass $m_{\tilde{\chi}_1^0}$ versus the lighter stau mass $m_{\tilde{\tau}_1}$ plane (middle), and the lightest neutralino mass $m_{\tilde{\chi}_1^0}$ versus the lightest chargino mass $m_{\tilde{\chi}_1^\pm}$ plane (right). The main annihilation mechanisms for the samples are indicated by their colors: yellow samples correspond to $\tilde{\tau}\tilde{\chi}_1^0$ coannihilation, blue samples represent $\tilde{\chi}_1^\pm\tilde{\chi}_1^0$ coannihilation, green samples correspond to $\tilde{\chi}_1^0\tilde{\chi}_1^\pm$ coannihilation, and red samples indicate $\tilde{\chi}_1^0$ annihilation. The following conclusions can be drawn:

- By comparing the upper middle and right panels of Fig.3, along with the left panel of Fig.5, it is evident that the primary annihilation mechanisms vary between classes:
 - In **Class A** and **Class C**, $\tilde{\chi}_1^0\tilde{\chi}_1^\pm$ coannihilation dominates, reflecting the tendency of wino-like $\tilde{\chi}_1^0$ to engage in this mechanism.
 - In **Class B**, $\tilde{\tau}\tilde{\chi}_1^0$ coannihilation is the main mechanism, characteristic of bino-like $\tilde{\chi}_1^0$.

TABLE II. Detailed information for the four surviving benchmark samples.

| | P1 | P2 | P3 | P4 |
|--|---------|---------|---------|--------|
| $\tan \beta$ | 12.63 | 9.59 | 5.81 | 12.88 |
| A_0 [GeV] | -4540.0 | -9491.1 | 3812.3 | -623.3 |
| M_0 [GeV] | 582.3 | 790.1 | 990.2 | 216.9 |
| M_1 [GeV] | 595.0 | 786.2 | 303.7 | 646.8 |
| M_2 [GeV] | 347.8 | 828.5 | 99.0 | 945.0 |
| M_3 [GeV] | 1586.7 | -6091.1 | -5387.8 | 2276.6 |
| μ [GeV] | 2803.7 | 5850.1 | 6165.0 | 2581.0 |
| m_h [GeV] | 125.6 | 123.8 | 123.2 | 123.1 |
| m_A [GeV] | 2779.4 | 5915.4 | 6315.2 | 2619.0 |
| $m_{\tilde{t}_1}$ [GeV] | 1814.0 | 8551.1 | 7412.2 | 3318.0 |
| $m_{\tilde{\tau}_1}$ [GeV] | 397.3 | 416.0 | 897.1 | 273.6 |
| $m_{\tilde{\mu}_1}$ [GeV] | 616.9 | 805.4 | 916.6 | 314.1 |
| $m_{\tilde{\nu}_e}$ [GeV] | 614.1 | 883.0 | 913.1 | 605.1 |
| $m_{\tilde{\nu}_\tau}$ [GeV] | 530.3 | 747.5 | 905.3 | 605.1 |
| $m_{\tilde{\chi}_1^\pm}$ [GeV] | 272.2 | 865.6 | 193.1 | 759.1 |
| $Br(B_s \rightarrow \mu^+ \mu^-)[10^{-9}]$ | 3.19 | 3.18 | 3.18 | 3.18 |
| $Br(B \rightarrow \tau \nu)[10^{-4}]$ | 0.837 | 0.837 | 0.837 | 0.836 |
| $Br(B \rightarrow s \gamma)[10^{-4}]$ | 3.330 | 3.354 | 3.355 | 3.377 |
| $\Delta a_\mu^{SUSY}[10^{-10}]$ | 3.98 | 1.90 | 0.61 | 6.49 |
| $m_{\tilde{\chi}_1^0}$ [GeV] | 248.4 | 406.0 | 170.9 | 267.1 |
| $m_{\tilde{\chi}_2^0}$ [GeV] | 270.4 | 813.1 | 189.8 | 716.2 |
| $\sigma_{SI}[10^{-48} \text{ cm}^2]$ | 10.7 | 1.03 | 5.13 | 5.34 |
| $\sigma_P^{SD}[10^{-46} \text{ cm}^2]$ | 25.1 | 0.61 | 2.04 | 13.3 |
| $\sigma_N^{SD}[10^{-46} \text{ cm}^2]$ | 50.2 | 0.835 | 2.39 | 21.3 |
| Ωh^2 | 0.109 | 0.114 | 0.118 | 0.113 |

- When $\tilde{\chi}_1^0$ exhibits bino-wino mixing, the dominant mechanism depends on the masses of $\tilde{\chi}_1^0$ and $\tilde{\chi}_1^\pm$, alternating between $\tilde{\chi}_1^\pm \tilde{\chi}_1^0$ coannihilation and $\tilde{\chi}_1^0$ annihilation.
- From the middle and right panels of Fig. 5, it is observed that for samples with non-degenerate masses of $\tilde{\tau}$ and $\tilde{\chi}_1^0$, annihilation mechanisms include $\tilde{\chi}_1^\pm \tilde{\chi}_1^0$ coannihilation, $\tilde{\chi}_1^0 \tilde{\chi}_1^\pm$ coannihilation, and $\tilde{\chi}_1^0$ annihilation. These mechanisms depend on the masses

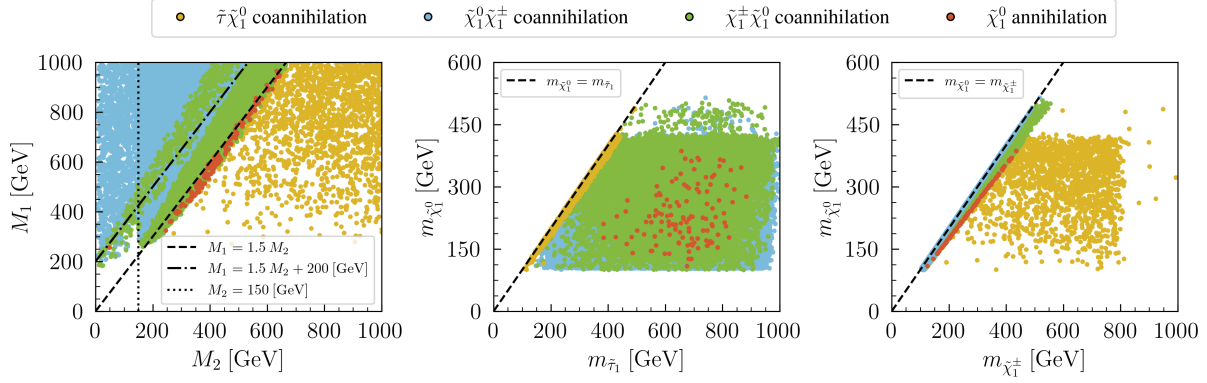


FIG. 5. Surviving samples in the M_1 versus M_2 planes (left), the lightest neutralino mass $m_{\tilde{\chi}_1^0}$ versus lighter stau mass $m_{\tilde{\tau}_1}$ plane (middle), and the lightest neutralino mass $m_{\tilde{\chi}_1^0}$ versus the lightest chargino mass $m_{\tilde{\chi}_1^\pm}$ plane (right). The main annihilation mechanisms for the samples are indicated by their colors: yellow samples correspond to $\tilde{\tau}\tilde{\chi}_1^0$ coannihilation, blue samples represent $\tilde{\chi}_1^\pm\tilde{\chi}_1^0$ coannihilation, green samples correspond to $\tilde{\chi}_1^0\tilde{\chi}_1^\pm$ coannihilation, and red samples indicate $\tilde{\chi}_1^0$ annihilation.

of $\tilde{\chi}_1^0$ and $\tilde{\chi}_1^\pm$, aligning with theoretical expectations.

In Fig. 6, the surviving samples are shown in the rescaled spin-independent (SI) DM-nucleon cross-section σ_{SI} (rescaled by Ω/Ω_0) versus $m_{\tilde{\chi}_1^0}$. In the left panel, the colors represent the dark matter relic density Ωh^2 . In the right panel, the colors indicate the primary annihilation mechanisms: yellow for $\tilde{\tau}\tilde{\chi}_1^0$ coannihilation, blue for $\tilde{\chi}_1^\pm\tilde{\chi}_1^0$ coannihilation, green for $\tilde{\chi}_1^0\tilde{\chi}_1^\pm$ coannihilation, and red for $\tilde{\chi}_1^0$ annihilation. The red solid curve shows the spin-independent DM-nucleon cross-section detection limits from LZ in 2022 [80]. The black dotted, red dot-dashed, and green dashed curves represent future detection limits from PandaX-xT (200t.y) [90], the projected LZ [91], and XENONnT (20t.y) [92], respectively. The gray shaded region indicates the neutrino floor [93]. The following conclusions can be drawn:

- All surviving samples predict a smaller rescaled σ_{SI} , with most falling below the detection limits of LZ 2022. From the left panel of Fig. 7, it can be seen that samples with larger Ωh^2 tend to predict larger rescaled σ_{SI} , while those dominated by $\tilde{\chi}_1^0$ annihilation predict very small rescaled σ_{SI} , all of which fall below the neutrino floor.
- By combining Fig. 6 with Fig. 4 in Ref. [94] and Fig. 5 in Ref. [95], one can observe

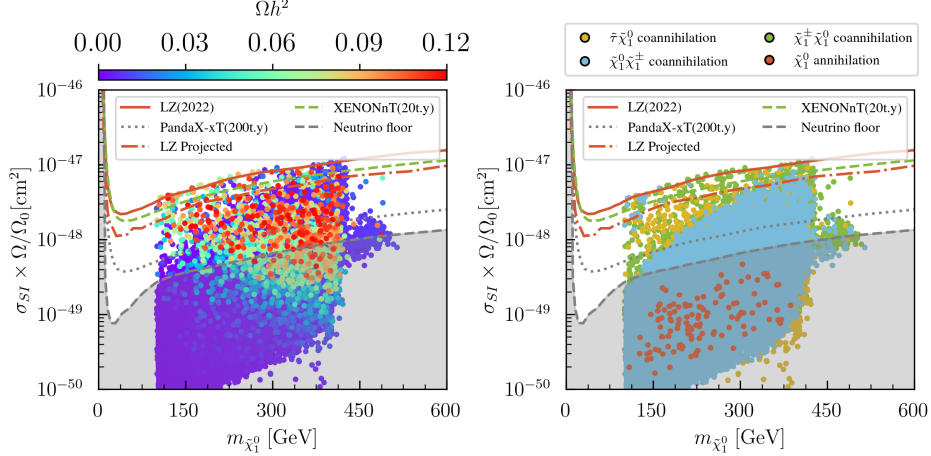


FIG. 6. Surviving samples in the rescaled spin independence (SI) DM-nucleon cross-section σ_{SI} (rescaled by Ω/Ω_0) versus $m_{\tilde{\chi}_1^0}$ panels. For the left panel, colors indicate dark matter relic density Ωh^2 . For the right panel, the main annihilation mechanisms of yellow samples are $\tilde{\tau}\tilde{\chi}_1^0$ coannihilation, the main annihilation mechanisms of blue samples are $\tilde{\chi}_1^\pm\tilde{\chi}_1^\pm$ coannihilation, the main annihilation mechanisms of green samples are $\tilde{\chi}_1^0\tilde{\chi}_1^\pm$ coannihilation, and the main annihilation mechanisms of red samples are $\tilde{\chi}_1^0$ annihilation. The red solid curves indicate the spin-independent (SI) DM-nucleon cross-section detection limits of LZ (2022) [80]. The black dotted, red dot-dashed, and green dashed curves indicate the future detection limits PandaX-xT(200t.y) [90], LZ Projected [91], and XENONnT(20t.y) [92], respectively. The gray shaded region indicated the neutrino floor [93].

that, compared to the higgsino-like dark matter, the bion-like dark matter tends to predict a significantly smaller rescaled σ_{SI} .

- Even with future dark matter detection experiments such as PandaX-xT (200t.y), the LZ Projected, and XENONnT (20t.y), it will remain difficult to cover all surviving samples. Many samples lie below the neutrino floor, making them nearly undetectable by dark matter experiments and requiring examination in collider experiments.

In Fig. 7, the surviving samples are presented in the M_1 versus M_2 planes (left), the lightest neutralino mass $m_{\tilde{\chi}_1^0}$ versus the lighter stau mass $m_{\tilde{\tau}_1}$ planes (middle) and $m_{\tilde{\chi}_1^0}$ versus the lighter chargino mass $m_{\tilde{\chi}_1^\pm}$ planes (right). The colors indicate the expected signal strength ratio r , calculated by SModelS-3.0.0 [85–87]. The right panel highlights the coverage of cur-

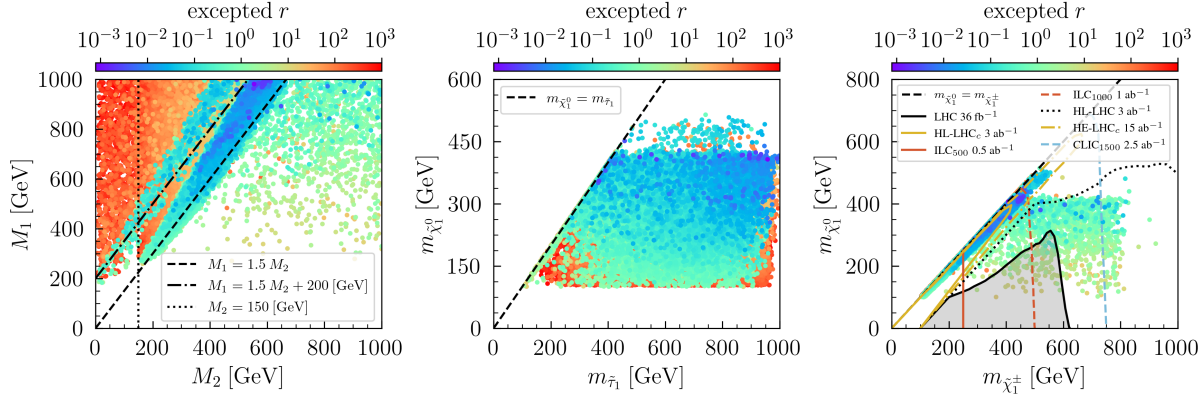


FIG. 7. Surviving samples in the M_1 versus M_2 planes (left), the lightest neutralino mass $m_{\tilde{\chi}_1^0}$ versus the lighter stau mass $m_{\tilde{\tau}_1}$ planes (middle) and $m_{\tilde{\chi}_1^0}$ versus the lighter chargino mass $m_{\tilde{\chi}_1^\pm}$ planes (right) with Colors indicate the expected r of signal strength. The black, yellow, and red solid curves of the right panel indicate the detection limits at LHC with 36 fb^{-1} [96, 97], HL-LHC compressed (HL-LHC_c) with 3 ab^{-1} [98], and 500 GeV International Linear Collider (ILC) with 0.5 ab^{-1} [99], respectively. The red dashed, black dotted, yellow dot-dashed, and green dashed curves indicate the future detectors of 1000 GeV ILC with 1 ab^{-1} [99], HL-LHC with 3 ab^{-1} [98], HE-LHC compressed (HE-LHC_c) with 15 ab^{-1} [100] and 1500 GeV Compact Linear Collider (CLIC₁₅₀₀) with 2.5 ab^{-1} [101]. The samples with smaller values of expected r are projected on top of larger ones.

rent and future collider experiments, including the LHC, High-Luminosity LHC (HL-LHC), High-Energy LHC (HE-LHC), the International Linear Collider (ILC), and the Compact Linear Collider (CLIC) [102]. Specifically, the black, yellow, and red solid curves of the right panel indicate the detection limits at LHC with 36 fb^{-1} [96, 97], HL-LHC compressed (HL-LHC_c) with 3 ab^{-1} [98], and 500 GeV International Linear Collider (ILC) with 0.5 ab^{-1} [99], respectively. The red dashed, black dotted, yellow dot-dashed, and green dashed curves indicate the future detectors of 1000 GeV ILC with 1 ab^{-1} [99], HL-LHC with 3 ab^{-1} [98], HE-LHC compressed (HE-LHC_c) with 15 ab^{-1} [100] and 1500 GeV Compact Linear Collider (CLIC₁₅₀₀) with 2.5 ab^{-1} [101]. Moreover, samples with smaller values of the expected r are projected on top of those with larger values. One can draw several conclusions from Fig. 7:

- Since an expected r of signal strength greater than 1 is considered excluded by the experiment, it can be observed from the left panel of Fig. 7 that the expected r values in **Class A** and **Class C** are relatively large. This indicates that direct searches

for supersymmetric particles impose strong constraints on these classes. In contrast, such constraints are weaker for **Class B** and the region where **Class A** and **Class B** intersect.

- Combining the left panel of Fig. 6 and the left panel of Fig. 7, an interesting observation can be made. The samples in **Class A** and **Class C** with $\tilde{\chi}_1^0\tilde{\chi}_1^\pm$ coannihilation exhibit small expected r values of signal strength. This indicates that, although direct searches for supersymmetric particles impose strong constraints on wino-like $\tilde{\chi}_1^0$ samples, these constraints become significantly weaker for wino-like samples with $\tilde{\chi}_1^0\tilde{\chi}_1^\pm$ coannihilation.
- From the middle and right panels of Fig. 7, it can be observed that direct searches for supersymmetric particles impose strong constraints primarily on two scenarios: (1) when $\tilde{\tau}_1$ is light and the masses of $\tilde{\tau}_1$ and $\tilde{\chi}_1^0$ are not degenerate, and (2) when the masses of $\tilde{\chi}_1^0$ and $\tilde{\chi}_1^\pm$ are degenerate. In other cases, these constraints are significantly weaker.
- From the right panel of Fig. 7, it can be observed that hadron colliders, including the LHC, HL-LHC, and HE-LHC, have very limited constraints on the compressed mass interval of the samples. Even with increased energy and luminosity, it remains challenging to cover all of these samples. In contrast, lepton colliders, such as the ILC and CLIC, demonstrate significantly better coverage in this region. They can effectively probe almost all samples with masses less than half of their collision energy, even with relatively modest integral luminosities. Overall, when the HL-LHC achieves an integral luminosity of 3 ab^{-1} and the CLIC₁₅₀₀ reaches 2.5 ab^{-1} , all surviving samples will be fully covered by these experiments.

IV. CONCLUSIONS

We investigated non-universal gaugino masses within an SU(5) GUT framework to reconcile the CMSSM with current experimental data. In particular, we focused on the \tilde{g} -SUGRA scenario, where $|M_3| \gg |M_1|, |M_2|$, so that the gluino mass significantly exceeds the masses of the other gauginos. Our analysis shows that precise Higgs data restricts the parameter

space by requiring $\tan\beta \gtrsim 5$ and $M_0 \gtrsim 20 \tan\beta \text{ GeV}$. Moreover, negative M_3 typically favors a lighter Higgs boson, whereas positive M_3 tends to yield a heavier one.

A substantial supersymmetric contribution to the muon anomalous magnetic moment $(g-2)_\mu$ demands both light sleptons and large $\tan\beta$, yet combining small M_0 with high $\tan\beta$ often makes it challenging to achieve a 125 GeV Higgs. Nevertheless, this framework can still accommodate the muon $(g-2)$ anomaly. We also observed that negative M_3 raises M_1^{SUSY} or M_2^{SUSY} through renormalization-group running, whereas positive M_3 lowers them. Depending on the ratio of M_1 to M_2 , the lightest neutralino $\tilde{\chi}_1^0$ can be wino-like, bino-like, or a wino-bino mixture; only bino-like states typically yield a larger dark matter relic density.

Concerning dark matter annihilation, the primary channels include stau annihilation, neutralino–stau coannihilation, neutralino–chargino coannihilation, and neutralino–neutralino annihilation. While these processes efficiently reduce the dark matter relic abundance, many samples predict extremely small spin-independent scattering cross sections σ_{SI} , sometimes below the neutrino floor, making them difficult to probe via direct detection experiments. On the other hand, future collider searches hold strong prospects for testing this scenario: once the High-Luminosity LHC reaches 3 ab^{-1} and CLIC₁₅₀₀ achieves 2.5 ab^{-1} , the entire parameter space—including the wino-like region—can be thoroughly examined. Our results thus indicate that the \tilde{g} -SUGRA scenario provides a consistent resolution to the CMSSM tension, offering clear, testable predictions for collider experiments.

ACKNOWLEDGMENTS

Yabo Dong thanks Rui Zhu for helpful discussion. This work was supported by the National Natural Science Foundation of China under Grant No. 12275066 and by the startup research funds of Henan University.

-
- [1] S. Chatrchyan *et al.* (CMS), *Phys. Lett. B* **716**, 30 (2012), [arXiv:1207.7235 \[hep-ex\]](#).
 - [2] G. Aad *et al.* (ATLAS), *Phys. Lett. B* **716**, 1 (2012), [arXiv:1207.7214 \[hep-ex\]](#).
 - [3] A. Tumasyan *et al.* (CMS), *Nature* **607**, 60 (2022), [Erratum: *Nature* 623, (2023)], [arXiv:2207.00043 \[hep-ex\]](#).

- [4] G. Aad *et al.* (ATLAS), *Nature* **607**, 52 (2022), [Erratum: *Nature* 612, E24 (2022)], [arXiv:2207.00092 \[hep-ex\]](#).
- [5] T. Aoyama *et al.*, *Phys. Rept.* **887**, 1 (2020), [arXiv:2006.04822 \[hep-ph\]](#).
- [6] D. P. Aguillard *et al.* (Muon g-2), *Phys. Rev. Lett.* **131**, 161802 (2023), [arXiv:2308.06230 \[hep-ex\]](#).
- [7] G. W. Bennett *et al.* (Muon g-2), *Phys. Rev. D* **73**, 072003 (2006), [arXiv:hep-ex/0602035](#).
- [8] B. Abi *et al.* (Muon g-2), *Phys. Rev. Lett.* **126**, 141801 (2021), [arXiv:2104.03281 \[hep-ex\]](#).
- [9] S. Navas *et al.* (Particle Data Group), *Phys. Rev. D* **110**, 030001 (2024).
- [10] N. Aghanim *et al.* (Planck), *Astron. Astrophys.* **641**, A6 (2020), [Erratum: *Astron. Astrophys.* 652, C4 (2021)], [arXiv:1807.06209 \[astro-ph.CO\]](#).
- [11] U. Chattopadhyay and P. Nath, *Phys. Rev. D* **53**, 1648 (1996), [arXiv:hep-ph/9507386](#).
- [12] S. Baek, N. G. Deshpande, X. G. He, and P. Ko, *Phys. Rev. D* **64**, 055006 (2001), [arXiv:hep-ph/0104141](#).
- [13] U. Chattopadhyay and P. Nath, *Phys. Rev. Lett.* **86**, 5854 (2001), [arXiv:hep-ph/0102157](#).
- [14] F. Wang, L. Wu, Y. Xiao, J. M. Yang, and Y. Zhang, *Nucl. Phys. B* **970**, 115486 (2021), [arXiv:2104.03262 \[hep-ph\]](#).
- [15] P. Cox, C. Han, and T. T. Yanagida, *Phys. Rev. D* **104**, 075035 (2021), [arXiv:2104.03290 \[hep-ph\]](#).
- [16] R. Dermisek, K. Hermanek, and N. McGinnis, *Phys. Rev. D* **104**, 055033 (2021), [arXiv:2103.05645 \[hep-ph\]](#).
- [17] K. Wang, J. Zhu, and Q. Jie, *Chin. Phys. C* **45**, 041003 (2021), [arXiv:2011.12848 \[hep-ph\]](#).
- [18] K. Wang and J. Zhu, *JHEP* **06**, 078 (2020), [arXiv:2002.05554 \[hep-ph\]](#).
- [19] J. M. Yang and Y. Zhang, *Sci. Bull.* **67**, 1430 (2022), [arXiv:2204.04202 \[hep-ph\]](#).
- [20] J. Kawamura, S. Okawa, and Y. Omura, *Phys. Rev. D* **106**, 015005 (2022), [arXiv:2204.07022 \[hep-ph\]](#).
- [21] M. Chakraborti, S. Iwamoto, J. S. Kim, R. Maselek, and K. Sakurai, *JHEP* **08**, 124 (2022), [arXiv:2202.12928 \[hep-ph\]](#).
- [22] S. Iguro, T. Kitahara, M. S. Lang, and M. Takeuchi, *Phys. Rev. D* **108**, 115012 (2023), [arXiv:2304.09887 \[hep-ph\]](#).
- [23] W. Li, H. Qiao, K. Wang, and J. Zhu, (2023), [arXiv:2312.17523 \[hep-ph\]](#).
- [24] K. Wang and J. Zhu, *Chin. Phys. C* **47**, 013107 (2023), [arXiv:2112.14576 \[hep-ph\]](#).

- [25] K. Wang and J. Zhu, *Phys. Rev. D* **101**, 095028 (2020), [arXiv:2003.01662 \[hep-ph\]](#).
- [26] F. Wang, K. Wang, J. M. Yang, and J. Zhu, *JHEP* **12**, 041 (2018), [arXiv:1808.10851 \[hep-ph\]](#).
- [27] M. Dine, A. E. Nelson, and Y. Shirman, *Phys. Rev. D* **51**, 1362 (1995), [arXiv:hep-ph/9408384](#).
- [28] J. M. Maldacena, *Adv. Theor. Math. Phys.* **2**, 231 (1998), [arXiv:hep-th/9711200](#).
- [29] H. E. Haber, *Nucl. Phys. B Proc. Suppl.* **101**, 217 (2001), [arXiv:hep-ph/0103095](#).
- [30] G. Jungman, M. Kamionkowski, and K. Griest, *Phys. Rept.* **267**, 195 (1996), [arXiv:hep-ph/9506380](#).
- [31] M. Carena, M. Quiros, and C. E. M. Wagner, *Nucl. Phys. B* **461**, 407 (1996), [arXiv:hep-ph/9508343](#).
- [32] H. E. Haber, *Nucl. Phys. B Proc. Suppl.* **62**, 469 (1998), [arXiv:hep-ph/9709450](#).
- [33] A. Djouadi *et al.* (MSSM Working Group), in *GDR (Groupement De Recherche) - Supersymetrie* (1998) [arXiv:hep-ph/9901246](#).
- [34] G. F. Giudice, A. Notari, M. Raidal, A. Riotto, and A. Strumia, *Nucl. Phys. B* **685**, 89 (2004), [arXiv:hep-ph/0310123](#).
- [35] J.-J. Cao, Z.-X. Heng, J. M. Yang, Y.-M. Zhang, and J.-Y. Zhu, *JHEP* **03**, 086 (2012), [arXiv:1202.5821 \[hep-ph\]](#).
- [36] A. Arbey, M. Battaglia, A. Djouadi, and F. Mahmoudi, *JHEP* **09**, 107 (2012), [arXiv:1207.1348 \[hep-ph\]](#).
- [37] T. Hahn, S. Heinemeyer, W. Hollik, H. Rzehak, and G. Weiglein, *Phys. Rev. Lett.* **112**, 141801 (2014), [arXiv:1312.4937 \[hep-ph\]](#).
- [38] M. Carena, S. Heinemeyer, O. Stål, C. E. M. Wagner, and G. Weiglein, *Eur. Phys. J. C* **73**, 2552 (2013), [arXiv:1302.7033 \[hep-ph\]](#).
- [39] M. Beneke, A. Bharucha, F. Dighera, C. Hellmann, A. Hryczuk, S. Recksiegel, and P. Ruiz-Femenia, *JHEP* **03**, 119 (2016), [arXiv:1601.04718 \[hep-ph\]](#).
- [40] V. Khachatryan *et al.* (CMS), *JHEP* **10**, 129 (2016), [arXiv:1606.03577 \[hep-ex\]](#).
- [41] M. Dugan, B. Grinstein, and L. J. Hall, *Nucl. Phys. B* **255**, 413 (1985).
- [42] J. A. Bagger, T. Moroi, and E. Poppitz, *JHEP* **04**, 009 (2000), [arXiv:hep-th/9911029](#).
- [43] J. R. Ellis, T. Falk, G. Ganis, K. A. Olive, and M. Srednicki, *Phys. Lett. B* **510**, 236 (2001), [arXiv:hep-ph/0102098](#).
- [44] P. Bechtle *et al.*, *PoS EPS-HEP2013*, 313 (2013), [arXiv:1310.3045 \[hep-ph\]](#).

- [45] C. Han, K.-i. Hikasa, L. Wu, J. M. Yang, and Y. Zhang, *Phys. Lett. B* **769**, 470 (2017), [arXiv:1612.02296 \[hep-ph\]](#).
- [46] G. Bélanger, J. Da Silva, and H. M. Tran, *Phys. Rev. D* **95**, 115017 (2017), [arXiv:1703.03275 \[hep-ph\]](#).
- [47] P. Athron *et al.* (GAMBIT), *Eur. Phys. J. C* **77**, 879 (2017), [arXiv:1705.07917 \[hep-ph\]](#).
- [48] P. Bechtle *et al.*, *Eur. Phys. J. C* **76**, 96 (2016), [arXiv:1508.05951 \[hep-ph\]](#).
- [49] J. Ellis and K. A. Olive, *Eur. Phys. J. C* **72**, 2005 (2012), [arXiv:1202.3262 \[hep-ph\]](#).
- [50] D. Ghosh, M. Guchait, S. Raychaudhuri, and D. Sengupta, *Phys. Rev. D* **86**, 055007 (2012), [arXiv:1205.2283 \[hep-ph\]](#).
- [51] H. P. Nilles, *Phys. Rept.* **110**, 1 (1984).
- [52] A. H. Chamseddine, R. L. Arnowitt, and P. Nath, *Phys. Rev. Lett.* **49**, 970 (1982).
- [53] R. Barbieri, S. Ferrara, and C. A. Savoy, *Phys. Lett. B* **119**, 343 (1982).
- [54] L. J. Hall, J. D. Lykken, and S. Weinberg, *Phys. Rev. D* **27**, 2359 (1983).
- [55] T. Li and D. V. Nanopoulos, *Phys. Lett. B* **692**, 121 (2010), [arXiv:1002.4183 \[hep-ph\]](#).
- [56] E. Bagnaschi *et al.*, *Eur. Phys. J. C* **77**, 268 (2017), [arXiv:1612.05210 \[hep-ph\]](#).
- [57] V. Khachatryan *et al.* (CMS), *Eur. Phys. J. C* **75**, 325 (2015), [arXiv:1502.02522 \[hep-ex\]](#).
- [58] T. Moroi and L. Randall, *Nucl. Phys. B* **570**, 455 (2000), [arXiv:hep-ph/9906527](#).
- [59] K. I. Izawa, Y. Nomura, K. Tobe, and T. Yanagida, *Phys. Rev. D* **56**, 2886 (1997), [arXiv:hep-ph/9705228](#).
- [60] Y. Kats, P. Meade, M. Reece, and D. Shih, *JHEP* **02**, 115 (2012), [arXiv:1110.6444 \[hep-ph\]](#).
- [61] S. Akula, B. Altunkaynak, D. Feldman, P. Nath, and G. Peim, *Phys. Rev. D* **85**, 075001 (2012), [arXiv:1112.3645 \[hep-ph\]](#).
- [62] S. Akula, P. Nath, and G. Peim, *Phys. Lett. B* **717**, 188 (2012), [arXiv:1207.1839 \[hep-ph\]](#).
- [63] G. Anderson, H. Baer, C.-h. Chen, and X. Tata, *Phys. Rev. D* **61**, 095005 (2000), [arXiv:hep-ph/9903370](#).
- [64] N. Chamoun, C.-S. Huang, C. Liu, and X.-H. Wu, *Nucl. Phys. B* **624**, 81 (2002), [arXiv:hep-ph/0110332](#).
- [65] J. Chakraborty and A. Raychaudhuri, *Phys. Lett. B* **673**, 57 (2009), [arXiv:0812.2783 \[hep-ph\]](#).
- [66] S. P. Martin, *Phys. Rev. D* **89**, 035011 (2014), [arXiv:1312.0582 \[hep-ph\]](#).
- [67] J. Kawamura and Y. Omura, *Phys. Rev. D* **93**, 055019 (2016), [arXiv:1601.03484 \[hep-ph\]](#).

- [68] A. S. Belyaev, S. F. King, and P. B. Schaefer, *Phys. Rev. D* **97**, 115002 (2018), [arXiv:1801.00514 \[hep-ph\]](#).
- [69] F. Wang, W. Wang, and J. M. Yang, *JHEP* **06**, 079 (2015), [arXiv:1504.00505 \[hep-ph\]](#).
- [70] S. Akula and P. Nath, *Phys. Rev. D* **87**, 115022 (2013), [arXiv:1304.5526 \[hep-ph\]](#).
- [71] A. Djouadi, J.-L. Kneur, and G. Moultaka, *Comput. Phys. Commun.* **176**, 426 (2007), [arXiv:hep-ph/0211331](#).
- [72] S. Chatrchyan *et al.* (CMS), *Phys. Lett. B* **716**, 30 (2012), [arXiv:1207.7235 \[hep-ex\]](#).
- [73] G. Aad *et al.* (ATLAS), *Phys. Lett. B* **716**, 1 (2012), [arXiv:1207.7214 \[hep-ex\]](#).
- [74] G. Aad *et al.* (ATLAS), *Eur. Phys. J. C* **76**, 6 (2016), [arXiv:1507.04548 \[hep-ex\]](#).
- [75] V. Khachatryan *et al.* (CMS), *Eur. Phys. J. C* **75**, 212 (2015), [arXiv:1412.8662 \[hep-ex\]](#).
- [76] A. M. Sirunyan *et al.* (CMS), *JHEP* **10**, 019 (2017), [arXiv:1706.04402 \[hep-ex\]](#).
- [77] S. Schael *et al.* (ALEPH, DELPHI, L3, OPAL, SLD, LEP Electroweak Working Group, SLD Electroweak Group, SLD Heavy Flavour Group), *Phys. Rept.* **427**, 257 (2006), [arXiv:hep-ex/0509008](#).
- [78] P. Bechtle, S. Heinemeyer, T. Klingl, T. Stefaniak, G. Weiglein, and J. Wittbrodt, *Eur. Phys. J. C* **81**, 145 (2021), [arXiv:2012.09197 \[hep-ph\]](#).
- [79] P. Bechtle, D. Dercks, S. Heinemeyer, T. Klingl, T. Stefaniak, G. Weiglein, and J. Wittbrodt, *Eur. Phys. J. C* **80**, 1211 (2020), [arXiv:2006.06007 \[hep-ph\]](#).
- [80] J. Aalbers *et al.* (LZ), *Phys. Rev. Lett.* **131**, 041002 (2023), [arXiv:2207.03764 \[hep-ex\]](#).
- [81] G. Belanger, F. Boudjema, A. Pukhov, and A. Semenov, *Comput. Phys. Commun.* **149**, 103 (2002), [arXiv:hep-ph/0112278](#).
- [82] G. Belanger, F. Boudjema, A. Pukhov, and A. Semenov, *Nuovo Cim. C* **033N2**, 111 (2010), [arXiv:1005.4133 \[hep-ph\]](#).
- [83] P. Athron, M. Bach, H. G. Fargnoli, C. Gnendiger, R. Greifenhagen, J.-h. Park, S. Paßehr, D. Stöckinger, H. Stöckinger-Kim, and A. Voigt, *Eur. Phys. J. C* **76**, 62 (2016), [arXiv:1510.08071 \[hep-ph\]](#).
- [84] P. Athron, C. Balazs, A. Cherchiglia, D. H. J. Jacob, D. Stöckinger, H. Stöckinger-Kim, and A. Voigt, *Eur. Phys. J. C* **82**, 229 (2022), [arXiv:2110.13238 \[hep-ph\]](#).
- [85] S. Kraml, S. Kulkarni, U. Laa, A. Lessa, W. Magerl, D. Proschofsky-Spindler, and W. Waltenberger, *Eur. Phys. J. C* **74**, 2868 (2014), [arXiv:1312.4175 \[hep-ph\]](#).
- [86] F. Ambrogio, S. Kraml, S. Kulkarni, U. Laa, A. Lessa, V. Magerl, J. Sonneveld, M. Traub,

- and W. Waltenberger, *Comput. Phys. Commun.* **227**, 72 (2018), [arXiv:1701.06586 \[hep-ph\]](#).
- [87] G. Alguero, J. Heisig, C. K. Khosa, S. Kraml, S. Kulkarni, A. Lessa, H. Reyes-González, W. Waltenberger, and A. Wongel, *JHEP* **08**, 068 (2022), [arXiv:2112.00769 \[hep-ph\]](#).
- [88] T. Moroi, *Phys. Rev. D* **53**, 6565 (1996), [Erratum: *Phys.Rev.D* 56, 4424 (1997)], [arXiv:hep-ph/9512396](#).
- [89] M. Endo, K. Hamaguchi, T. Kitahara, and T. Yoshinaga, *JHEP* **11**, 013 (2013), [arXiv:1309.3065 \[hep-ph\]](#).
- [90] A. Abdukerim *et al.* (PandaX), (2024), [arXiv:2402.03596 \[hep-ex\]](#).
- [91] D. S. Akerib *et al.* (LZ), *Phys. Rev. D* **101**, 052002 (2020), [arXiv:1802.06039 \[astro-ph.IM\]](#).
- [92] E. Aprile *et al.* (XENON), *JCAP* **11**, 031 (2020), [arXiv:2007.08796 \[physics.ins-det\]](#).
- [93] J. Billard, L. Strigari, and E. Figueroa-Feliciano, *Phys. Rev. D* **89**, 023524 (2014), [arXiv:1307.5458 \[hep-ph\]](#).
- [94] K. Wang and J. Zhu, *Chin. Phys. C* **48**, 113101 (2024), [arXiv:2406.15939 \[hep-ph\]](#).
- [95] J. Zhao, J. Zhu, P. Zhu, and R. Zhu, *Phys. Rev. D* **107**, 055030 (2023), [arXiv:2211.14587 \[hep-ph\]](#).
- [96] M. Aaboud *et al.* (ATLAS), *Phys. Rev. D* **97**, 112001 (2018), [arXiv:1712.02332 \[hep-ex\]](#).
- [97] V. Khachatryan *et al.* (CMS), *Eur. Phys. J. C* **77**, 294 (2017), [arXiv:1611.00338 \[hep-ex\]](#).
- [98] M. Aaboud *et al.* (ATLAS), ATL-PHYS-PUB-2014-010 (2014).
- [99] M. Berggren, in *International Workshop on Future Linear Colliders* (2020) [arXiv:2003.12391 \[hep-ph\]](#).
- [100] X. Cid Vidal *et al.*, *CERN Yellow Rep. Monogr.* **7**, 585 (2019), [arXiv:1812.07831 \[hep-ph\]](#).
- [101] J. de Blas *et al.* (CLIC), **3/2018** (2018), 10.23731/CYRM-2018-003, [arXiv:1812.02093 \[hep-ph\]](#).
- [102] R. K. Ellis *et al.*, (2019), [arXiv:1910.11775 \[hep-ex\]](#).